A constitutive model accounting for strain ageing effects on work-hardening. Application to a C–Mn steel

Sicong Ren, Matthieu Mazière, Samuel Forest, Thilo F. Morgeneyer, Gilles Rousselier

A constitutive model accounting for strain ageing effects on work-hardening. Application to a C–Mn steel

Sicong Ren, Matthieu Mazière *, Samuel Forest, Thilo F. Morgeneyer, Gilles Rousselier

MINES ParisTech, PSL Research University, MAT–Centre des matériaux, CNRS UMR 7633, BP 87, 91003 Évry, France

A B S T R A C T

One of the most successful models for describing the Portevin–Le Chatelier effect in engineering applications is the Kubin–Estrin–McCormick model (KEMC). In the present work, the influence of dynamic strain ageing on dynamic recovery due to dislocation annihilation is introduced in order to improve the KEMC model. This modification accounts for additional strain hardening rate due to limited dislocation annihilation by the diffusion of solute atoms and dislocation pinning at low strain rate and/or high temperature. The parameters associated with this novel formulation are identified based on tensile tests for a C–Mn steel at seven temperatures ranging from $20\,^\circ$C to $350\,^\circ$C. The validity of the model and the improvement compared to existing models are tested using 2D and 3D finite element simulations of the Portevin–Le Chatelier effect in tension.

© 2017 Académie des sciences. Published by Elsevier Masson SAS. This is an open access article under the CC BY-NC-ND license (http://creativecommons.org/licenses/by-nc-nd/4.0/).

1. Introduction

Serrated flow and propagating plastic strain localisation bands are salient features of the Portevin–Le Chatelier (PLC) effect, which is observed during tensile tests in many industrial metallic alloys within a given range of strain rates and temperatures. It has been reported in alloys containing substitutional atoms, such as Al–Cu alloys [1–4], Al–Mg alloys [5–8], or involving interstitial elements like carbon in steels [9,10]. It has also been observed in nickel- [11,12] and titanium-based [13] alloys. The PLC effect is usually associated with a negative strain rate sensitivity (nSRS) of the flow stress, which means that the latter decreases when the prescribed strain rate increases. Besides the abnormal flow stress, the localisation of strain into Lüders or PLC bands and the negative strain rate sensitivity, some other severe changes in mechanical properties have been reported within the PLC active domain, such as loss of toughness and ductility [9,14–19]. Some authors have shown that the strain localisation associated with the PLC effect promotes the initiation of cracks and consequently results in a reduced material toughness in fracture mechanics CT specimens [10]. In contrast, the authors in [20] noticed a reduction of the strain for initiation of necking in smooth tensile specimens, but they did not report any decrease of the strain to failure. The main parameter controlling the occurrence of necking and the subsequent final failure is the hardening rate. A proper description of the coupling between strain ageing and hardening is therefore necessary to explain the deterioration in mechanical properties within the PLC domain.

At the microscopic scale, it is widely accepted that the PLC effect in alloys is caused by dynamic strain ageing (DSA), which refers to the interaction between mobile dislocations and the diffusion of solute atoms. Cottrell and Bilby [21] were the first to interpret PLC effects based on the DSA mechanism. The interaction was assumed to take place between continuously moving dislocations and a solute atmosphere. Later, Penning [22] investigated several important aspects of the PLC effect from a mathematical point of view, including the propagative localised plastic deformation band, the influence of machine stiffness and, most importantly, the necessity of negative strain rate sensitivity. These two pioneering works set the basis for the development of DSA models accounting for the PLC effect. Van den Beukel [23] took into account the discontinuous motion of dislocations in the DSA model by introducing the waiting time t_w of the dislocations arrested at obstacles. During the waiting time, solute atoms diffuse towards the arrested dislocations, and an over-stress is required to trigger further dislocation motion. The movement of an unpinned dislocation to the next obstacle is assumed to be almost instantaneous: this flying time is negligible compared with the waiting time. Kubin and Estrin [24,25] proposed a relation between the waiting time and the strain rate, which has been widely used in works [26,27]. The critical conditions for the onset of the PLC effect were discussed in detail by these authors. McCormick [28] further developed a complete mechanical model accounting for the transient behaviour observed during strain rate jump tests by underlying the difference between the effective ageing time t_a and waiting time t_w.

The KEMC model as proposed by McCormick [28] and Kubin and Estrin [24] is based on the introduction in the total flow stress of an over-stress due to dynamic strain ageing and depending on the ageing time t_a. This over-stress is maximal for low strain rates, high temperatures, or large values of the initial ageing time. Since the ageing time evolution depends on the waiting time t_w, which depends itself on the plastic strain rate, the ageing over-stress is an implicit function of the latter, allowing the modelling of the negative strain rate sensitivity. The KEMC model predicts both Lüders and Portevin–Le Chatelier instabilities, as it can be noticed in numerous works using this model for finite element simulations [3,9,26,27, 29–31]. In the original version of the KEMC model [28] and in many of the following studies [26,29], the waiting time t_w is also assumed to be a function of the plastic strain. Since the number of obstacles increases with plastic strain, the waiting time should grow as well. On the contrary, the maximum over-stress level due to strain ageing is assumed to be independent of the plastic deformation. Finally, in the KEMC model, dynamic strain ageing only has a limited influence on the hardening rate with evolving prescribed strain rate. In some alloys, however, such as C–Mn steels, the influence of DSA on the strain hardening rate is rather strong [9]. This interaction has also been observed in magnesium alloys [32], cobalt-based superalloys [33], or in nickel-based superalloys [34].

In addition to the original KEMC model, dislocation dynamics-based models for DSA and PLC have been recently proposed [35–37]. Strain hardening is then controlled by the dislocation density evolution, divided into a production and an annihilation term. In [36], the model accounts for a single population of dislocations. It is rather similar to the original KEMC model, since the over-stress is added to the total flow stress and increases consequently, but DSA has almost no influence on the hardening rate. On the contrary, in [35] and [37], an indirect coupling between strain ageing and strain hardening is proposed in a model based on two different dislocation populations (mobile and forest dislocations). The coupling between strain ageing and strain hardening is introduced by an increase of the forest dislocation density in order to represent the "probability of dislocation pinning by solute atoms at some obstacles such as forest dislocations". The model proposed in [35] and [37] is, however, rather complex, with a large number of parameters to identify. On the other hand, the original KEMC model was modified by Böhlke et al. in [3] to account for the influence of DSA on the hardening rate by introducing a strain-dependent maximal value of the over-stress due to strain ageing (σ_{B0} in [3]). This modification of the original KEMC model is purely phenomenological and mainly motivated by a better description of the critical plastic strain for PLC in aluminium alloys. The same approach has been used in some following articles to account for the interaction between strain ageing and strain hardening [31,33].

To achieve the goal of a better description of the experimental hardening rate within a simple and physically sound model, the idea of the present work is to propose a modification of the hardening rate by the impediment of the annihilation of dislocation segments by solute atoms. This dislocation mechanism has actually been observed in TEM observations as shown in [38,39]. The objective of the present work is therefore to formulate a modified Kocks–Mecking model into which DSA effects are introduced in the yield function like in [36], but also in the dynamic recovery term of the dislocation density evolution. The advantages of this constitutive model will be highlighted.

The work is organised as follows. The theoretical considerations about the new model are presented in section 2. The dislocation evolution law is separated into the multiplication and annihilation parts. The influence of strain ageing is introduced in the dislocation annihilation term. A systematic identification procedure is provided in section 3 to calibrate the material parameters for a C–Mn steel tested at several strain rates from room temperature to 350 °C. However, a model accounting for DSA is valid only if serrations are predicted within the accurate strain rate domain. For that purpose, finite element simulations must be performed for the whole specimens and not only at the material volume element level. In section 4, validation tests are then carried out and presented using the identified material model for 2D and 3D finite element meshes.

2. Formulation of the constitutive model

The proposed constitutive model is presented within the finite strain framework using the concept of local objective frames following [40]. The second and fourth order tensors are defined by a single tilde $\underset{\sim}{\Box}$ and a double tilde $\underset{\approx}{\Box}$, respectively.

Observer invariant stress and strain rate measures $\underset{\sim}{\sigma}$ and $\underset{\sim}{\dot{\varepsilon}}$ are defined by the transformation of the Cauchy stress tensor $\underset{\sim}{T}$ and the Eulerian strain rate tensor $\underset{\sim}{D}$ into the corotational frame characterized by the rotation $\underset{\sim}{Q}$ $(\underline{x},t)$ at each material point:

$$
\begin{cases}
\underset{\sim}{\sigma} = \underset{\sim}{Q} . \underset{\sim}{T} . \underset{\sim}{Q}^{\mathrm{T}} \\
\underset{\sim}{\dot{\varepsilon}} = \underset{\sim}{Q} . \underset{\sim}{D} . \underset{\sim}{Q}^{\mathrm{T}} \\
\underset{\sim}{Q} \quad \text{such as} \quad \underset{\sim}{\dot{Q}}^{\mathrm{T}} . \underset{\sim}{Q} = \underset{\sim}{\Omega} \quad \text{(corotational)}
\end{cases}
$$

where $\underset{\sim}{D}$ and $\underset{\sim}{\Omega}$ respectively are the symmetric and skew-symmetric parts of the velocity gradient.

2.1. Constitutive equations

The strain rate is then decomposed into elastic and plastic parts:

$$
\underset{\sim}{\dot{\varepsilon}} = \underset{\sim}{\dot{\varepsilon}}^e + \underset{\sim}{\dot{\varepsilon}}^p, \quad \underset{\sim}{\sigma} = \underset{\approx}{C} : \underset{\sim}{\varepsilon}^e \tag{1}
$$

where $\underset{\approx}{C}$ is the Hooke tensor of elasticity. The plastic flow is described by the normality rule

$$
\underset{\sim}{\dot{\varepsilon}}^p = \dot{p}\,\underset{\sim}{n}, \quad \underset{\sim}{n} = \frac{\partial f}{\partial \underset{\sim}{\sigma}} \tag{2}
$$

where p is the cumulative plastic strain and the yield function, f, is taken in the form

$$
f(\underset{\sim}{\sigma}, \rho, t_a) = \sigma_{eq}(\underset{\sim}{\sigma}) - R(\rho) - R_a(t_a) \tag{3}
$$

In the previous equation, σ_{eq} is the equivalent stress measure. The threshold for yielding is the sum $R(\rho) + R_a(t_a)$ where $R(\rho)$ is the usual yield stress depending on the total dislocation density ρ and $R_a(t_a)$ is the yield stress enhancement (over-stress) due to ageing.

In addition, an hyperbolic flow rule is introduced in the current model that accounts for the thermal activation phenomenon:

$$
\dot{p} = \dot{\varepsilon}_0 \exp\left(-\frac{E_a}{k_B T}\right) \sinh\left(\frac{V_a \langle f \rangle}{k_B T}\right) \tag{4}
$$

where $\langle f \rangle = \max(f, 0)$. The threshold strain rate at which thermal activation takes place is $\dot{\varepsilon}_0$ and k_B and T are respectively the Boltzmann constant and the temperature in Kelvin. V_a and E_a are respectively the activation volume and the activation energy.

The last term $R_a(t_a)$ on the right side of Eq. (3) is the yield over-stress due to strain ageing:

$$
R_a = P_1 \phi(t_a) \tag{5}
$$

with

$$
\phi(t_a) = 1 - \exp(-(t_a/t_0)^n) \tag{6}
$$

where $\phi(t_a)$ is the relative concentration of solute atoms pinning the dislocations. It varies between 0 and 1. $\phi = 1$ means that dislocations are totally pinned, while $\phi = 0$ corresponds to the unpinned case. P_1 is the maximal stress drop magnitude from the pinned state $\phi = 1$ to the unpinned state $\phi = 0$. The parameter t_0 is related to the diffusivity of solute atoms, see [36].

The ageing time t_a is defined by the following evolution law:

$$
\dot{t}_a = 1 - \frac{t_a}{t_w}, \quad t_w = \frac{w}{\dot{p}}, \quad t_a(t=0) = t_{a0} \tag{7}
$$

where t_w denotes the average waiting time of dislocations at obstacles. It is worth noting that t_a is equal to the waiting time t_w only for the steady state [28]. The initial time t_{a0} is related to the presence of static ageing. A proper initial time value allows a good description of Lüders peak and plateau. The parameter ω represents the strain increment produced when all arrested dislocations overcome local obstacles and move forward to the next pinned configuration.

The second term $R(\rho)$ on the right-hand side of Eq. (3) represents isotropic hardening, which is expressed in terms of the total dislocation density ρ:

$$
R(\rho) = \sigma_0 + \gamma \mu b \sqrt{\rho}, \quad R_0 = \sigma_0 + \gamma \mu b \sqrt{\rho_0} \tag{8}
$$

where μ is the shear modulus; γ is a material-scale parameter [41]; b is the magnitude of the Burgers vector. For the sake of simplicity, we do not distinguish between forest and mobile dislocation densities.

The evolution of dislocation density is based on a modified Kocks–Mecking equation [41]:

$$\dot{\rho} = \left(a_0 \sqrt{\rho} - b_0 (1 - \zeta \phi) \rho \right) \dot{p} \tag{9}$$

where the first term $a_0 \sqrt{\rho}$ on the right-hand side of Eq. (9) describes the multiplication of the dislocations. The second term $b_0 (1 - \zeta \phi) \rho \dot{p}$ is related to the annihilation (dynamic recovery) process for dislocation dipoles, which is considered to be affected by strain ageing. This coupling with strain ageing is absent in earlier formulations of the KEMC model. Physically, the short-range motion of dislocations required for annihilation or dynamic recovery is impeded by the trapping of solute atoms at dislocations (especially at low strain rates or high temperatures). Consequently, strain ageing reduces the ability of the material to exhibit dynamic recovery. In Eq. (9), the strain ageing influence on dynamic recovery depends on the current value of the function $\phi(t_a)$. When $\phi(t_a)$ is maximal, i.e. for low strain rates or high temperatures, the dynamic recovery process is significantly reduced by strain ageing, which results in a larger dislocation density production rate $\dot{\rho}$, and, accordingly, in a larger hardening rate. On the contrary, when $\phi(t_a)$ is minimal, i.e. for high strain rates or low temperatures, strain ageing has no influence on dislocation annihilation allowing for standard dynamic recovery and a reduced dislocation density growth rate $\dot{\rho}$ and associated hardening rate. Finally, the hardening rate will then be larger for low strain rates than for large strain rates, as experimentally observed [9]. The parameter ζ, $0 \le \zeta \le 1$, has to be identified in order to control the level of influence of strain ageing on strain hardening ($\zeta = 0$ means no influence, while $\zeta = 1$ the maximal influence).

2.2. New features in the macroscopic response of the new model

After introducing the ageing effect on dislocation annihilation and consequently in the isotropic hardening term $R(\rho)$, R_a is no longer the only term in the model responsible for dynamic strain ageing effects. This new feature of the model is now illustrated in the case of the C–Mn steel, for which the KEMC material parameters were previously identified, see [42].
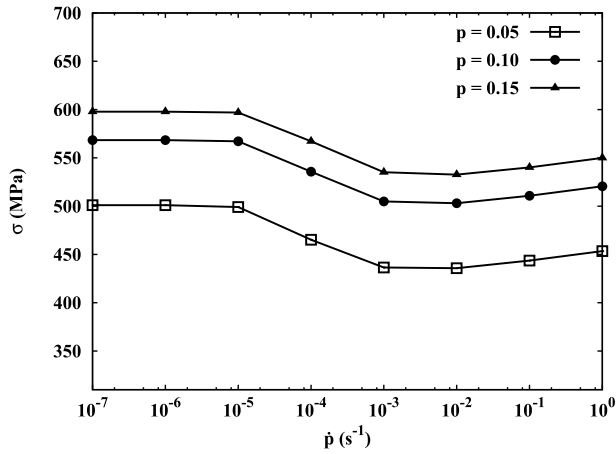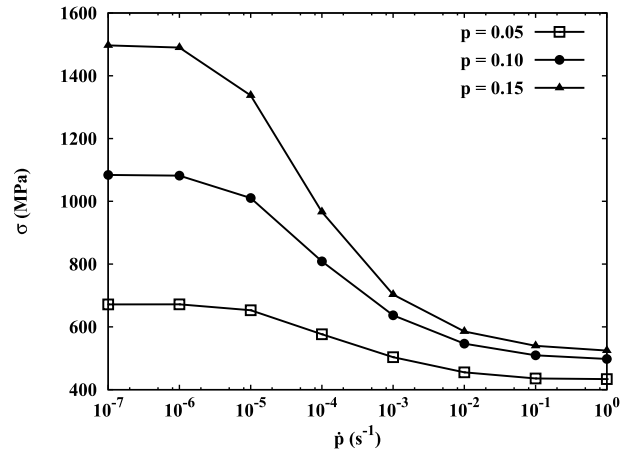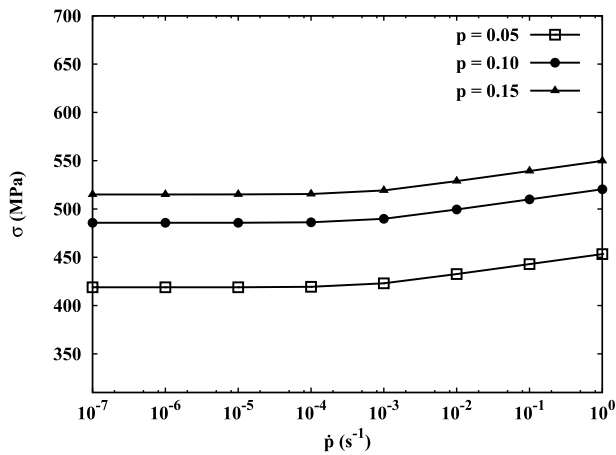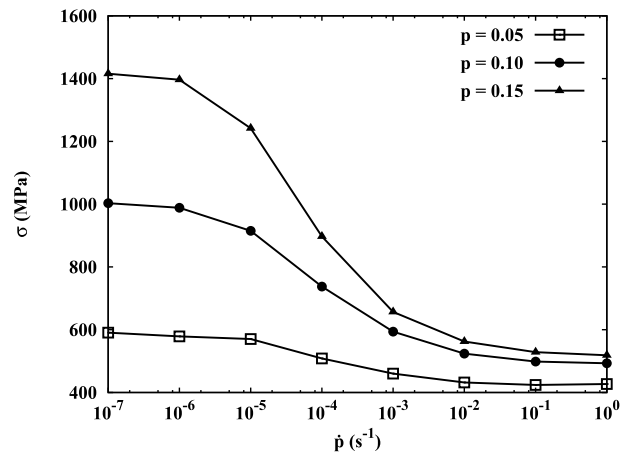
The modified model has been identified anew based on the same experimental curves as in [42]. This identification procedure is presented in section 3. In the present subsection, the main features of the model are illustrated by setting ζ to $\zeta = 1$ to enhance the effect. Actually, the optimal value $\zeta = 0.2$ was found for the current identification as shown in Table 2. The details about the identification will be presented in the next section.

The strain rate sensitivity of the models is investigated in Fig. 1, which shows the evolution of the 1D steady-state stress as a function of the plastic strain rate at three different plastic strain levels (0.05, 0.10, and 0.15) for the C–Mn steel using the original KEMC model and the novel formulation. The original version of the model is retrieved for $\zeta = 0$. The curves of Fig. 1(a) display the usual S-shape for strain-ageing materials. The role of the parameter P_1, see Eq. (5), is investigated. Four situations are considered in Fig. 1: $P_1 \neq 0, \zeta = 0$ (original KEMC model), $P_1 = 0, \zeta = 0$ (truncated KEMC model), $P_1 \neq 0, \zeta = 1$ (new model), $P_1 = 0, \zeta = 1$ (truncated new model). Setting $P_1 = 0$ amounts to killing the over-stress $R_a(t_a)$.
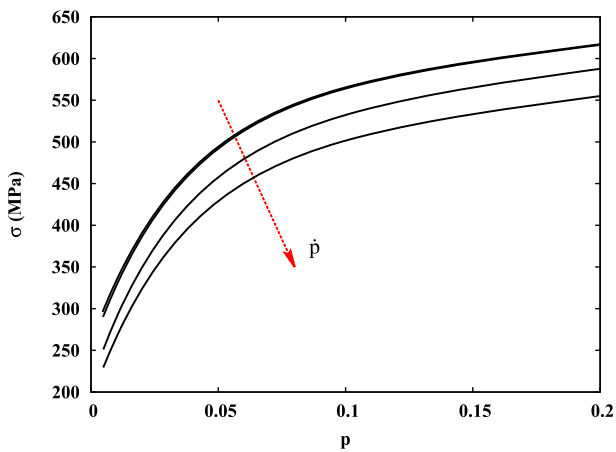
A negative strain rate sensitivity (nSRS) domain can be observed for the original as well as for the new model for the cases $P_1 \neq 0$, as shown in Fig. 1(a) and (b).

For $P_1 = 0$, see Fig. 1(c), a slight positive sensitivity can be observed, which indicates that the dynamic strain-ageing effect is completely eliminated for $P_1 = 0$ in the original KEMC model. On the contrary, the new model can still produce a negative strain-rate sensitivity, even for $P_1 = 0$, as shown in Fig. 1(d). Such a feature of the modified model can be particularly useful since, in the original KEMC model, the parameter $P_1 = 0$ controls simultaneously the amplitude of the serrations and the amplitude of the negative strain-rate sensitivity domain. These two amplitudes being for some materials (especially steels) different by one order of magnitude, a compromise has to be made in the parameter identification of the KEMC model. In the new model, the negative strain rate sensitivity is not only controlled by the R_a term, but is also induced by the coupling between strain ageing and strain hardening in Eq. (9). The material parameter P_1 can then be devoted to an accurate description of serrations only.
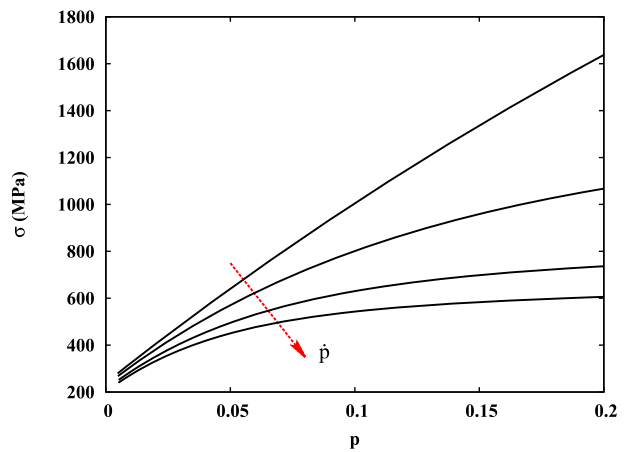
In Fig. 2, tensile stress–strain curves under various global prescribed strain rates predicted by the two models are compared. The red arrow indicates the direction of increasing applied strain rates. Both figures show the strain rate sensitive behaviour in the nSRS zone (i.e. between 10^{-5} and 10^{-1} s^{-1}). It can be noticed that the curves obtained by the original model at different strain rates are almost parallel to each other. This indicates that the evolution of the hardening rate is the same at each strain rate during straining (see Fig. 2(a)). In contrast, some experimental observations on C–Mn steels show that the distance between the curves increases with strain [9]. A better modelling of this effect was proposed by Böhlke et al. [3], who prescribed a linear increasing evolution for P_1 with respect to the cumulative plastic strain p. From a physical point of view, it is expected that the apparent hardening rate should also be influenced by strain ageing due to the interaction between dislocations perturbed by the pinning of segments. The proposed new model includes such an influence of strain ageing on the strain hardening rate, via the function $\zeta \phi$ in Eq. (9). The stress–strain curves produced by the modified model are close to each other at low strain, and spread at higher strain levels, which shows a strong similarity to the experimental results (see Fig. 4(a)) that will be presented in the next section.

(a) $P_1 \neq 0$ using the original model [42].

(b) $P_1 \neq 0$ using the new model with $\zeta = 1.0$.

(c) $P_1 = 0$ using the original model [42].

(d) $P_1 = 0$ using the new model with $\zeta = 1.0$.

Fig. 1. Strain rate sensitivity according to the original KEMC and new models for uniaxial tension under prescribed plastic strain rate. The corresponding stress is given at three distinct plastic-strain levels.
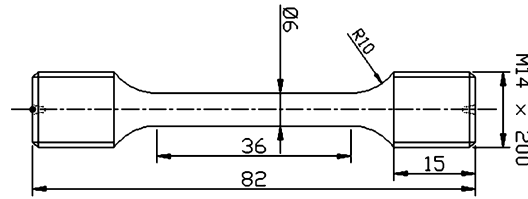

(a) KEMC model [42]

(b) the new model

Fig. 2. Comparison of the stress–strain curves for different applied strain rates $\dot{E}$.

Table 1
Chemical composition (mass fraction in %) of the C–Mn steel considered in the current study.

C	S	P	Si	Mn	Ni	Mo	Nb	V	Cu	Sn	N	Al
0.19	0.0074	0.011	0.27	1.07	0.04	0.01	< 0.01	< 0.01	0.05	< 0.05	0.011	0.0085

Fig. 3. Geometry of the round tensile specimens [10].

3. Identification of the new model for a C–Mn steel

3.1. Experiments

The considered C–Mn steel is used for the secondary system pipelines of pressurized water reactor (PWR) in nuclear power plants [43]. The chemical composition of this material (TU48C) is given in Table 1. Its tensile mechanical behaviour was characterized in the temperature range between 20 °C and 350 °C [9]. The interstitial atoms like carbon and nitrogen act as solid solute atoms and make this material sensitive to strain-ageing phenomena. The geometry of the round tensile specimens used for tensile testing are shown in Fig. 3.

Tensile tests were performed at seven temperatures from 20 °C to 350 °C. At each temperature, various strain rates from 10^{-2} to 10^{-4} s^{-1} (or 10^{-5} s^{-1}) were considered. The PLC effect is observed in the temperature range from 150 °C to 300 °C for the considered strain rates. Fig. 4 shows the stress–strain curves tested at 200 °C. A marked negative strain rate sensitivity and some serrated plastic flow (both Lüders and PLC effects) can be observed.

The first step of the identification strategy consists in smoothing the curves, thus eliminating the Lüders plateau and the PLC serrations, for the determination of the strain hardening parameters, see the dotted lines in Fig. 4(a). The hardening rates obtained from these smooth curves are presented in Fig. 4(b). The identification is based on the true stress–strain curves.

3.2. Identification

Several model parameters can be taken from the literature dealing with similar steels. The activation energy E_a in Eq. (4) is chosen to be 0.6 eV, and the parameter $\dot{\varepsilon}_0$ is equal to 6.2 s^{-1} according to [36]. The activation volume V_a is taken from [42].

The identification of the ageing term R_a (Eqs. (5), (6) and (7)) is the essential part and involves four distinct parameters: P_1, t_0, n, w. The initial ageing time, t_{a0}, must also be chosen. The parameter w remains constant with the value $2. \times 10^{-4}$ for all temperatures, referring to [9]. The parameter n can be fixed at 0.66 or 0.33, corresponding to bulk or pipe diffusion according to [44]. The latter value was found to provide better results in the current model for this material. In the current study, t_{a0} is in a first step of the identification set to 0 to exclude the initial Lüders effect. The other two parameters P_1 and t_0 are those that remain to be identified. In the isotropic hardening term, the Burgers vector b takes the value 0.29 nm and the initial dislocation density is $\rho_0 = 1.0 \times 10^7$ mm^{-2} [9].
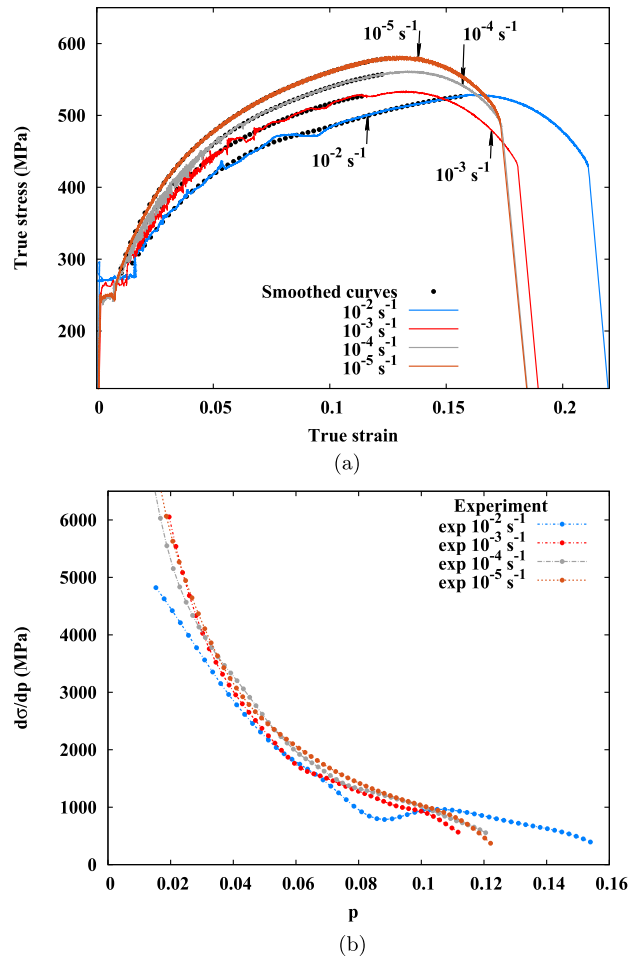
The next step consists in identifying the seven remaining parameters accounting for strain hardening behaviour, including σ_0, a_0, b_0, ζ, P_1, t_0.

An optimisation procedure using the Levenberg–Marquardt algorithm is used to minimize the deviation between data from material point simulations and that of the smoothed experimental stress–strain curves. This strategy avoids time-consuming FEM simulations on full-dimension specimens [36]. However, the localisation pattern related to strain ageing requires a field analysis and cannot be captured by volume element simulations. Simulations on full-size specimens are therefore necessary in a third step to validate the model identification and possibly adjust the parameter w.

The Table 2 provides the optimized parameters for all temperatures.

The results of the material parameter identification at 200 °C and 300 °C are plotted respectively in Figs. 5 and 6. The material point simulation responses are compared with the smoothed and truncated experimental curves for the original model as proposed by Wang et al. [9], and the new one.

As shown in Figs. 5 and 6, both models reproduce the effect of temperature and simulate the different levels of yield stress and hardening at different strain rates. However, it can be noticed that the distance between the experimental curves at different strain rates increases with strain, as mentioned in section 2.2. The original model does not capture this feature. In the original model, the ageing over-stress influences the yield stress in such a way that a pair of stress/strain curves

Fig. 4. (a) Experimental and smoothed tensile curves at 200 °C (reproduced from [42]) serve as initial data for model calibration. (b) Hardening rate evolution as a function of plastic strain under different strain rates.
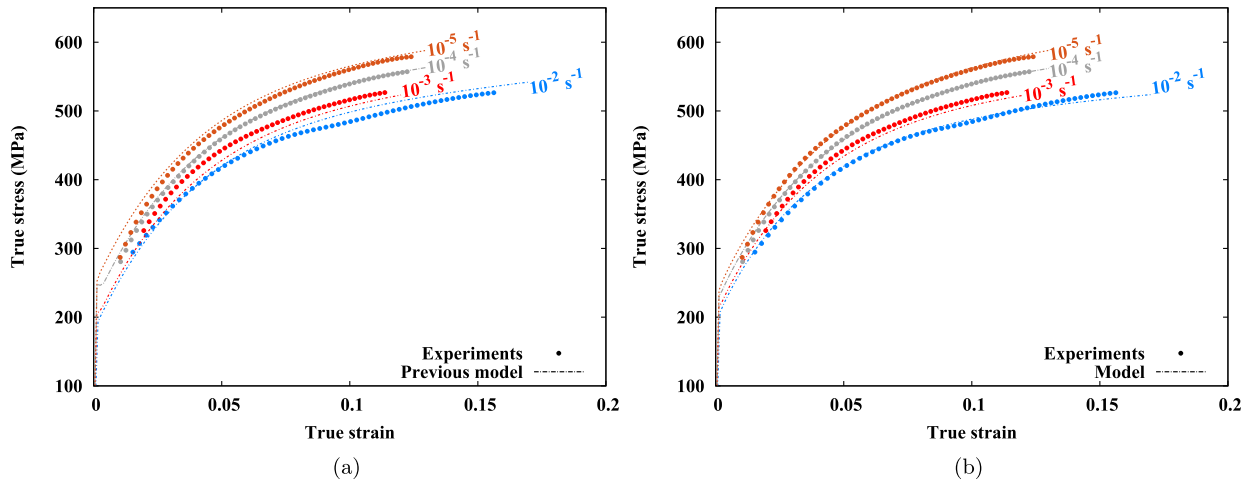
Table 2
Identified material parameters of the constitutive model.

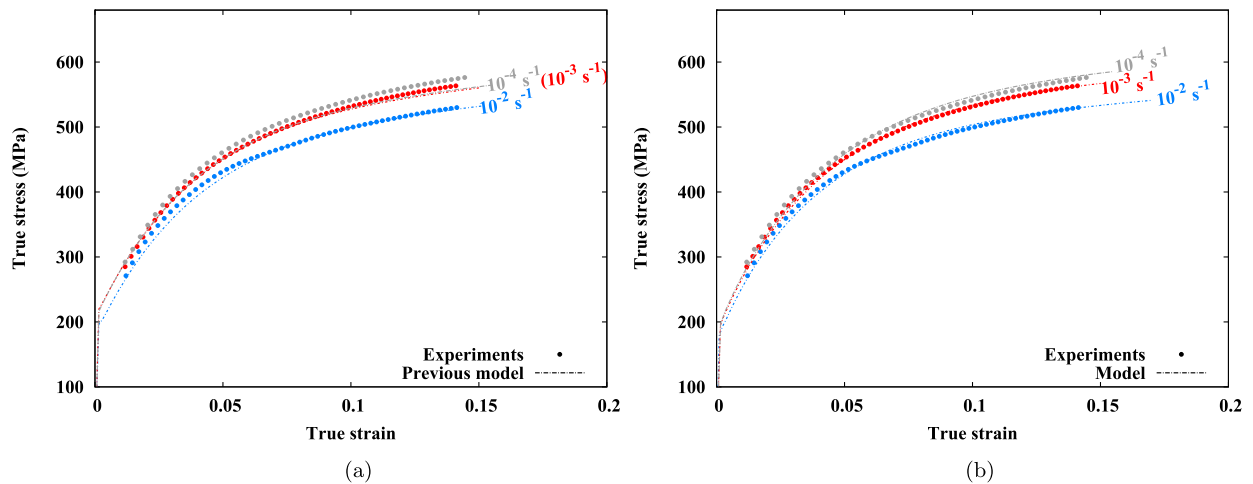| T (°C)	20	100	150	200	250	300	350
E (GPa)	210	205	201	198	195	192	188
v	0.3	0.3	0.3	0.3	0.3	0.3	0.3
σ_0 (MPa)	166	160	139	116	94	74	72
γ	0.3	0.3	0.3	0.3	0.3	0.3	0.3
b (mm)	2.9e−7	2.9e−7	2.9e−7	2.9e−7	2.9e−7	2.9e−7	2.9e−7
a_0	1.44e6	1.52e6	1.75e6	2.46e6	2.92e6	2.96e6	3.00e6
b_0	32.0	37.0	44.1	57.1	59.0	62.3	64.2
ζ	0.2	0.2	0.2	0.2	0.2	0.2	0.2
P_1 (MPa)	136	120	114	101	95.3	91.7	85.0
t_0 (s)	1.78e5	6.72e2	1.30e1	1.05	7.68e−1	3.89e−2	5.11e−3
ω	2.0e−4	2.0e−4	2.0e−4	2.0e−4	2.0e−4	2.0e−4	2.0e−4
n	0.33	0.33	0.33	0.33	0.33	0.33	0.33
ρ_0 (mm^{-2})	1.0e7	1.0e7	1.0e7	1.0e7	1.0e7	1.0e7	1.0e7
V_a (b^3)	43.29	48.60	53.46	58.82	64.19	69.01	73.87
E_a (eV)	0.6	0.6	0.6	0.6	0.6	0.6	0.6
$\dot{\varepsilon}$ (s^{-1})	6.2	6.2	6.2	6.2	6.2	6.2	6.2

for two different prescribed strain rates are simply translated by a given constant stress value. The hardening rate for each prescribed strain rate remains constant as shown in Fig. 7(a), which is not in agreement with the experimental results (see Fig. 4(b)).

In contrast, the dislocation density model proposed in this work, which includes a strain ageing influence on the dislocation annihilation rate accurately, accounts for this effect. As presented in Fig. 7(b), the hardening rate is different for

Fig. 5. (a) Identification results at 200 °C proposed by Wang et al. [9]. (b) Identification of the new model at 200 °C.

Fig. 6. (a) Identification results at 300 °C proposed by Wang et al. [9]. (b) Identification of the current model.

each prescribed strain rate using the current model. This result is close to the one plotted in Fig. 4(b), which gives the experimental hardening rate evolution curves as functions of the plastic strain.

3.3. Evolution of parameter t_0 with temperature

The material parameters have been identified independently for each temperature. It is however essential to check the evolution of parameters with temperature and possibly point out some possible Arrhenius dependence. This is checked here for the parameter t_0. Following the original work by Cottrell and Bilby [21], this parameter should have the following temperature dependence:

$$t_0(T) \propto \frac{T}{D(T)} \propto T \exp\left[\frac{Q_m}{k_B T}\right] \tag{10}$$

where $D(T)$ is the diffusion coefficient of solute atoms, and Q_m the activation energy of the diffusion process. Such a function has been fitted on the results of Table 2, as it can be seen from Fig. 8.

The parameter Q_m/k_B is found to be equal to 9880 K, which leads to $Q_m = 19.5$ kcal/mol, which is close to the value of $Q = 18.65$ kcal/mol estimated by Da Silva and McLellan in 1976 [46] for the diffusion of carbon in B.C.C. iron. The value estimated by the same author for the diffusion of nitrogen in B.C.C. iron is smaller and equal to 17.54 kcal/mol. This identification provides a clear physical basis to the proposed strain ageing equations.
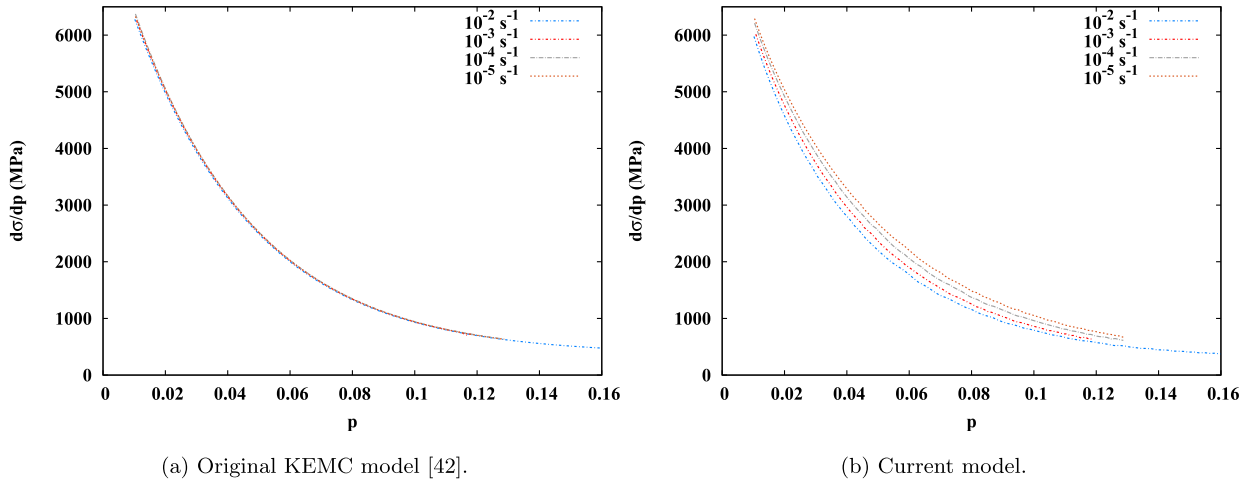
(a) Original KEMC model [42].

(b) Current model.

Fig. 7. Comparison of the hardening rate curves for the original KEMC model [45] and the current model at 200 °C.
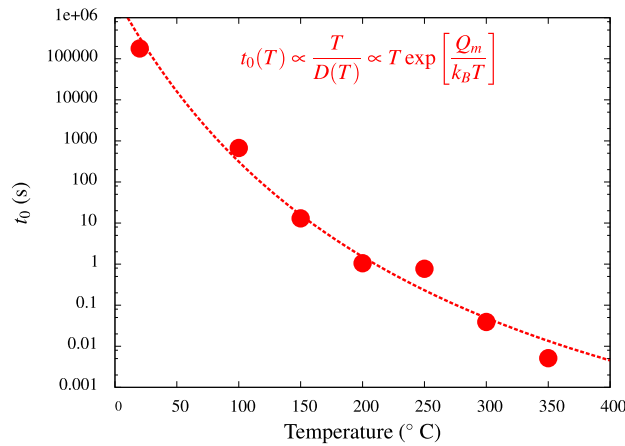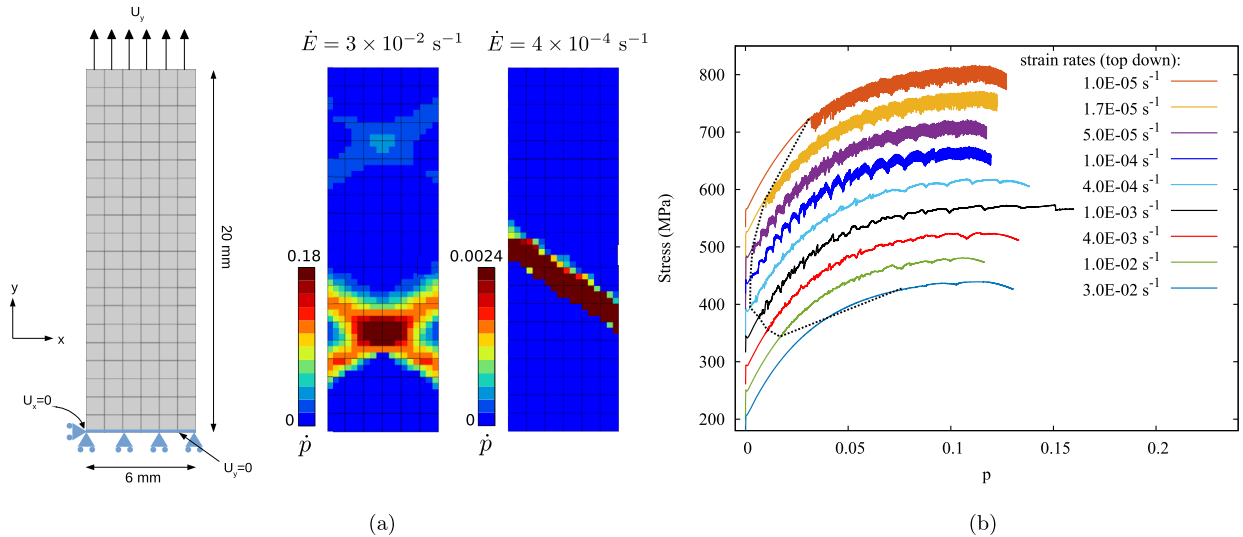

Fig. 8. Evolution of parameter t_0 with temperature and calibration of the associated activation energy.

4. Validation on 2D and 3D geometries

The previous identification was based on material point simulations and smoothed experimental curves. In order to verify the ability of the model to capture the localisation patterns, it must be tested on the whole real specimen geometry. Considering that the simulation on a 3D finite element mesh is time-consuming, a 2D mesh is firstly used for testing strain rate effects. A 2D rectangular plate with dimensions 6 mm × 20 mm used for uni-axial tension simulation is presented in Fig. 9(a). Axial displacement boundary conditions are prescribed to the upper and lower ends of the plate. Complementing displacement conditions are imposed to fix the rigid body motion. Plastic strain rate localisation bands are predicted at strain rates of 3×10^{-2} s^{-1} and 4×10^{-4} s^{-1}. They are shown in Fig. 9. The X-shaped strain rate localisation band is observed at $\dot{E} = 3 \times 10^{-2}$ s^{-1}. The simulation at lower strain rate leads to inclined localisation bands. Similar phenomenon has been reported in the literature [27].

Fig. 9(b) shows nine stress–strain curves simulated at 200 °C with different strain rates ranging from 1.0×10^{-5} s^{-1} to 3.0×10^{-2} s^{-1}. The shape of serrations can be seen to be strain rate dependent. The amplitude and the frequency of serrations decrease with the strain rate. This trend is in agreement with experimental observations (see Fig. 4). The strain-rate dependence of the frequency and size of the stress serrations has been discussed in [47].

Another important feature of the PLC effect is the critical condition for the occurrence of instabilities. This condition is usually measured by the critical plastic strain. Experimental observations show that the critical plastic strain strongly depends on the applied strain rate (see, e.g., [5,48]). A U-shape curve can be observed if the first significant stress drop is considered to estimate the critical strain (see dashed line in Fig. 9(b)). The U-shape curve shows that the unstable zone only occurs within a certain range of strain rates at a given temperature. The reason is beyond the scope of this paper. In fact, this phenomenon is well known and has been already discussed in some experimental [48] or numerical [49] papers.

Fig. 9. (a) Finite element mesh of a 2D plate; plastic strain rate bands for several prescribed strain rates. (b) Stress–strain curves over a large range of strain rates obtained by FEM simulations (plane stress) using the parameters identified at $T = 200\,°C$. The successive curves are shifted by 40 MPa for better illustration.

2D simulations are known to be prone to strain localisation, so that more realistic 3D simulations are necessary for the validation. Such 3D simulations are carried out on round tensile specimens at $T = 200\,°C$. The specimen is meshed with quadratic brick elements with reduced integration. The specimen geometry and boundary conditions are shown in Fig. 10(a). Simulations are conducted under two different macroscopic strain rates, $\dot{E} = 10^{-4}$ s^{-1} and $\dot{E} = 10^{-2}$ s^{-1}. For the simulation at strain rate $\dot{E} = 10^{-4}$ s^{-1}, inclined plastic strain rate $\dot{p}$ bands are observed, while conical ones are found at a higher strain rate, i.e. $\dot{E} = 10^{-2}$ s^{-1}. The rotation of slant bands travelling along the gauge length is a typical phenomenon (see Fig. 10(b)) observed in cylindrical specimens in the simulations. This effect may explain the spiral (double) shear lips found on the fracture surface [50]. The FEM tensile curve at $\dot{E} = 10^{-2}$ s^{-1}, together with the experimental curve, is plotted in Fig. 10(c). A good agreement with the experimental one is found.
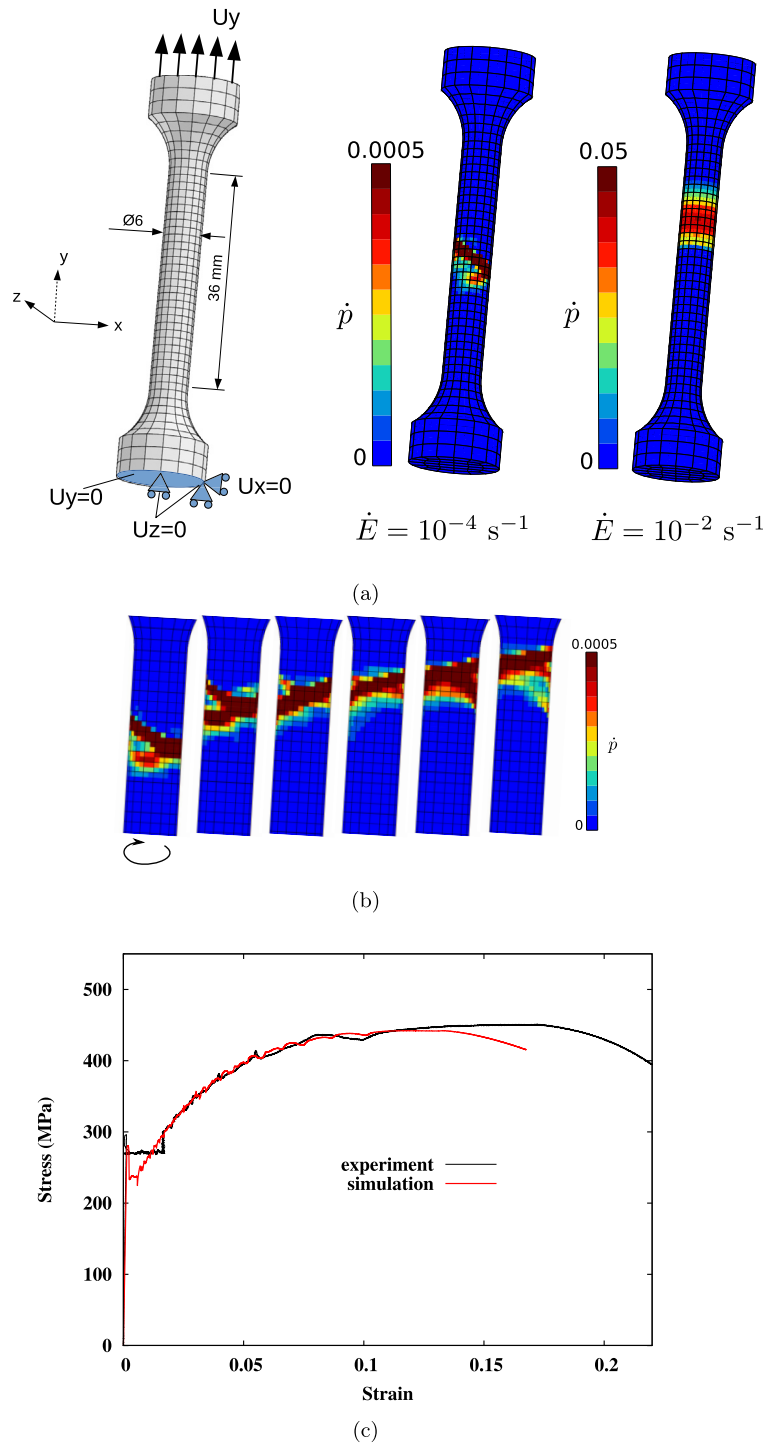
According to [36], a small perturbation of the boundary conditions can lead to a symmetry-breaking mode. This has been tested in the present study. A small transverse displacement $U_x = 0.1$ mm along the x-axis is applied to the upper surface of the cylindrical specimen. Fig. 11 displays both Lüders and PLC localisation bands, as shown by the plastic strain rate field $\dot{p}$ obtained at an overall strain rate $\dot{E} = 10^{-2}$ s^{-1}. The double Lüders bands formed at the plateau exhibit a conical shape in the absence of any perturbation (see Fig. 11(a)). In contrast, the symmetry of the Lüders bands is easily broken by the presence of a very small perturbation, as shown in Fig. 11(b). The PLC bands, however, remain conical (Fig. 11(c)). In addition, the mesh effect is apparent: the band width is approximately that of one layer of elements. A regularization procedure should be used in future work [51,52].

Fig. 12 shows the spatio-temporal graphs of the plastic strain rate of the 3D simulations presented in Fig. 10. The plastic strain rate is normalized by dividing the bulk strain rate ($\dot{p}/\dot{E}$). These graphs display the evolution of plastic strain rate versus time along the vertical line Y placed in the gauge area. It is obtained by extracting the plastic strain rate along line Y at each acquisition time (see Fig. 10(a)), which results in a file containing many data blocks corresponding to different acquisition times. Each data block is composed of the coordinates along the vertical direction and the plastic strain rate corresponding to each coordinate. Finally, these data are mapped on a 2D plane with a colour contour representing the normalized strain rate magnitude. The y axis gives the position of bands corresponding to each acquisition time (x-axis). It can be noted that the bands at $\dot{E} = 10^{-2}$ s^{-1} are typical type-A bands. The type-B bands are obtained at $\dot{E} = 10^{-4}$ s^{-1}.

It can also be noticed that the critical strain obtained by 3D simulations is different from that obtained with 2D ones. The 2D simulations are performed on a perfect rectangular plate. In contrast, 3D simulations are performed on a 3D round bar specimen with shoulders and heads. Simulations and experimental results show that the initiation of instabilities are usually located in the shoulders. This could explain the earlier triggering of PLC effect in 3D simulations. As shown in Fig. 13, the critical strain using an ideal cylindrical bar appears later than that obtained by a round bar specimen with shoulders.
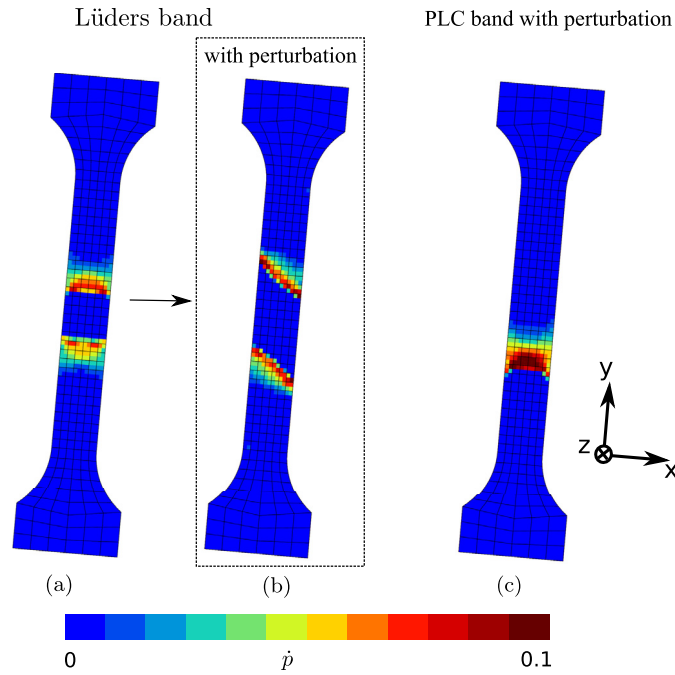
5. Conclusions

In this work, a dislocation-density-based modified Kubin–Estrin–McCormick (KEMC) model has been proposed in order to better describe the interaction between strain-hardening and strain-ageing phenomena. The coupling between dynamic strain ageing and strain hardening is accounted for by introducing a limitation of the dynamic recovery process due to DSA. This modification allows us to increase the hardening rate in the temperature and strain rate domain where the pinning of
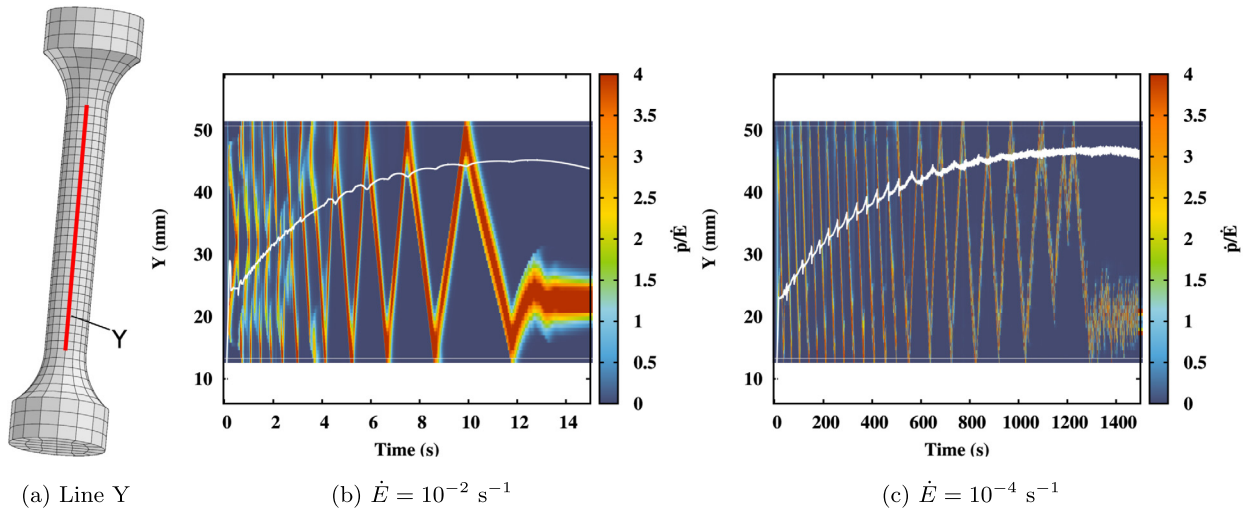
(a)

(b)

(c)

Fig. 10. (a) Mesh of a 3D round tensile specimen simulated at $T = 200\,^{\circ}$C: strain rate $\dot{p}$ bands at two different applied macroscopic strain rates ($\dot{E} = 10^{-4}$ and $\dot{E} = 10^{-2}$ s^{-1}); (b) band rotation at strain rate $\dot{E} = 10^{-4}$ s^{-1}; (c) comparison of the tensile curves at $\dot{E} = 10^{-2}$ s^{-1}.

dislocations by solute atoms is the most active, i.e. for low strain rates or high temperatures. The cost for the introduction of this coupling is rather low, since it requires no additional internal variable and only one additional material parameter ζ.

The new model formulation has been identified using material point simulations for a C–Mn steel over a large range of temperatures and strain rates. The results show a significant improvement on the description of hardening with respect to previous identifications. Serrations on the stress/strain curves as well as the associated plastic strain rate localisation bands have been reproduced and illustrated using 2D and 3D finite element simulations. One major advantage of the proposed

Fig. 11. Simulations of plastic strain rate bands at macroscopic strain rate $\dot{E} = 10^{-2}$ s^{-1} (view of the internal half plane cutting the round bar): (a) conical Lüders band without perturbation of the boundary conditions; (b) slant Lüders band when a small perturbation is applied in the x direction; (c) conical PLC bands when a small perturbation is applied.

Fig. 12. Spatio-temporal graphs corresponding to the simulation at strain rates $\dot{E} = 10^{-2}$ s^{-1} and $\dot{E} = 10^{-4}$ s^{-1}.

model compared to previous formulations including the evolution of various types of dislocation densities (e.g., [35,37]) is its relative simplicity, allowing for structural engineering finite element computations to be performed, as demonstrated by the 3D simulations in the present work. Furthermore, the limitation of the current model might be its ability to simulate complex thermomechanical paths like combinations of heat treatment and tension/compression/relaxation/creep loadings. In those cases, the more sophisticated model [35,37] might give more realistic results.

The modified model has been tested on a C–Mn steel for which the proposed interaction between dynamic strain ageing and strain hardening is clearly visible. The same work could be applied to some nickel-based superalloys [53] and some Al–Mg aluminium alloys [8], since the features of DSA and of the Portevin–Le Chatelier effect are very similar. It would probably be more difficult for certain aluminium alloys, such as 2000 series Al–Cu and Al–Cu–Li alloys, for which the negative strain rate sensitivity is not very pronounced, and some other phenomena than DSA can be responsible for serrated yielding [54].
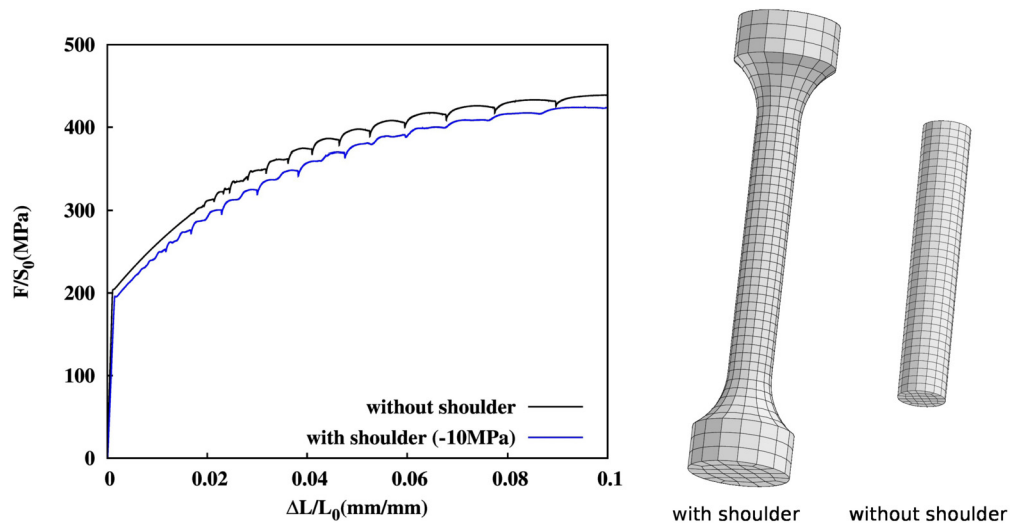
Fig. 13. 3D simulations using a cylindrical bar and a round bar specimen with shoulders at the same strain rate $\dot{E} = 10^{-2}$ s^{-1}.

Concerning C–Mn steels, the accuracy of the model could be tested using more advanced experimental devices like digital image correlation or digital image thermography, combined with a statistical analysis of stress drops. Such experimental information could then be compared with the results of finite element simulations. Finally, it would be relevant to use the modified model in order to investigate the failure of C–Mn steel in the DSA domain, and particularly the loss of ductility that is observed in this domain [9,43].

References

[1] Z.Y. Jiang, Q.C. Zhang, H.F. Jiang, Z.J. Chen, X.P. Wu, Spatial characteristics of the Portevin–Le Chatelier deformation bands in Al-4at% Cu polycrystals, Mater. Sci. Eng. A 403 (1) (2005) 154–164.

[2] N. Ranc, D. Wagner, Some aspects of Portevin–Le Chatelier plastic instabilities investigated by infrared pyrometry, Mater. Sci. Eng. A 394 (1) (2005) 87–95.

[3] T. Böhlke, G. Bondár, Y. Estrin, M.A. Lebyodkin, Geometrically non-linear modeling of the Portevin–Le Chatelier effect, Comput. Mater. Sci. 44 (4) (2009) 1076–1088.

[4] S.C. Ren, T.F. Morgeneyer, M. Mazière, S. Forest, G. Rousselier, Portevin–Le chatelier effect triggered by complex loading paths in an Al–Cu aluminium alloy. Submitted for publication.

[5] H. Dierke, F. Krawehl, S. Graff, S. Forest, J. Šachl, H. Neuhäuser, Portevin–Le Chatelier effect in Al–Mg alloys: influence of obstacles—experiments and modelling, Comput. Mater. Sci. 39 (1) (2007) 106–112.

[6] H. Louche, P. Vacher, R. Arrieux, Thermal observations associated with the Portevin–Le Chatelier effect in an Al–Mg alloy, Mater. Sci. Eng. A 404 (1) (2005) 188–196.

[7] R.C. Picu, G. Vincze, F. Ozturk, J.J. Gracio, F. Barlat, A.M. Maniatty, Strain rate sensitivity of the commercial aluminum alloy AA5182-O, Mater. Sci. Eng. A 390 (1) (2005) 334–343.

[8] H. Halim, D.S. Wilkinson, M. Niewczas, The Portevin–Le Chatelier (PLC) effect and shear band formation in an AA5754 alloy, Acta Mater. 55 (12) (2007) 4151–4160.

[9] H.D. Wang, C. Berdin, M. Mazière, S. Forest, C. Prioul, A. Parrot, P. Le-Delliou, Experimental and numerical study of dynamic strain ageing and its relation to ductile fracture of a C–Mn steel, Mater. Sci. Eng. A 547 (2012) 19–31.

[10] J. Belotteau, Comportement et rupture d'un acier au C–Mn en présence de vieillissement sous déformation, PhD dissertation, Ecole Centrale Paris, Paris, 2009.

[11] L. Fournier, D. Delafosse, T. Magnin, Oxidation induced intergranular cracking and Portevin–Le Chatelier effect in nickel base superalloy 718, Mater. Sci. Eng. A 316 (1) (2001) 166–173.

[12] K.B.S. Rao, S. Kalluri, G.R. Halford, M.A. McGaw, Serrated flow and deformation substructure at room temperature in inconel 718 superalloy during strain controlled fatigue, Scr. Metall. Mater. 32 (4) (1995) 493–498.

[13] K. Prasad, S.V. Kamat, Transient flow behaviour in a near alpha titanium alloy timetal 834 in the dynamic strain aging regime, Mater. Sci. Eng. A 490 (1) (2008) 477–480.

[14] J.K. Chakravartty, S.L. Wadekar, T.K. Sinha, M.K. Asundi, Dynamic strain-ageing of A203D nuclear structural steel, J. Nucl. Mater. 119 (1) (1983) 51–58.

[15] M.T. Miglin, W.A. Van Der Sluys, R.J. Futato, H.A. Domian, Effects of strain aging in the unloading compliance J test, in: Elastic–Plastic Fracture Test Methods: The User's Experience, ASTM International, 1985.

[16] P. Gomiero, Y. Bréchet, F. Louchet, A. Tourabi, B. Wack, Microstructure and mechanical properties of a 2091 AlLi alloy-III. Quantitative analysis of Portevin–Le Chatelier instabilities and relation to toughness in Al–Li, Al–Cu–Mg and Al–Li–Cu–Mg (2091) alloys, Acta Metall. Mater. 40 (4) (1992) 863–871.

[17] K.C. Kim, J.T. Kim, J.I. Suk, U.H. Sung, H. Kwon, Influences of the dynamic strain aging on the J–R fracture characteristics of the ferritic steels for reactor coolant piping system, Nucl. Eng. Des. 228 (1) (2004) 151–159.

[18] D. Wagner, J.C. Moreno, C. Prioul, Dynamic strain aging sensitivity of heat affected zones in C–Mn steels, J. Nucl. Mater. 252 (3) (1998) 257–265.

[19] E. Amar, A. Pineau, Interpretation of ductile fracture toughness temperature dependence of a low strength steel in terms of a local approach, Eng. Fract. Mech. 22(6) (6) (1985) 1061–1071.

[20] F. Zhang, A.F. Bower, W.A. Curtin, The influence of serrated flow on necking in tensile specimens, Acta Mater. 60 (2012) 43–50.

[21] A.H. Cottrell, B.A. Bilby, Dislocation theory of yielding and strain ageing of iron, Proc. Phys. Soc. 62 (1) (1949) 49.

[22] P. Penning, Mathematics of the Portevin–Le Chatelier effect, Acta Metall. Mater. 20 (10) (1972) 1169–1175.
[23] A. van den Beukel, Theory of the effect of dynamic strain aging on mechanical properties, Phys. Status Solidi 30 (1) (1975) 197–206.
[24] L.P. Kubin, Y. Estrin, The Portevin–Le Chatelier effect in deformation with constant stress rate, Acta Metall. Mater. 33 (3) (1985) 397–407.
[25] L.P. Kubin, Y. Estrin, Evolution of dislocation densities and the critical conditions for the Portevin–Le Chatelier effect, Acta Metall. Mater. 38 (5) (1990) 697–708.
[26] S. Graff, S. Forest, J.-L. Strudel, C. Prioul, P. Pilvin, J.-L. Béchade, Strain localization phenomena associated with static and dynamic strain ageing in notched specimens: experiments and finite element simulations, Mater. Sci. Eng. A 387 (2004) 181–185.
[27] M. Mazière, J. Besson, S. Forest, B. Tanguy, H. Chalons, F. Vogel, Numerical aspects in the finite element simulation of the Portevin–Le Chatelier effect, Comput. Methods Appl. Mech. Eng. 199 (9) (2010) 734–754.
[28] P.G. McCormick, Theory of flow localisation due to dynamic strain ageing, Acta Metall. Mater. 36 (12) (1988) 3061–3067.
[29] S. Zhang, P.G. McCormick, Y. Estrin, The morphology of Portevin–Le Chatelier bands: finite element simulation for Al–Mg–Si, Acta Mater. 49 (2001) 1087–1094.
[30] A. Benallal, T. Berstad, T. Borvik, O.S. Hopperstad, I. Koutiri, R. Nogueira de Codes, An experimental and numerical investigation of AA5083 aluminium alloy in presence of the Portevin–Le Chatelier effect, Int. J. Plast. 24 (2008) 1916–1945.
[31] B. Klusemann, G. Fischer, T. Boehlke, B. Svendsen, Thermomechanical characterization of Portevin–Le Chatelier bands in AlMg3 (AA5754) and modeling based on a modified Estrin–McCormick approach, Int. J. Plast. 67 (2015) 192–216.
[32] T.Q. Li, Y.B. Liu, Z.Y. Cao, D.M. Jiang, L.R. Cheng, The tensile properties and high cyclic fatigue characteristics of Mg-5Li-3Al-1.5Zn-2RE alloy, Mater. Sci. Eng. A 527 (2010) 7808–7811.
[33] J.-L. Chaboche, A. Gaubert, P. Kanouté, A. Longuet, F. Azzouz, M. Mazière, Viscoplastic constitutive equations of combustion chamber materials including cyclic hardening and dynamic strain aging, Int. J. Plast. 46 (2013) 1–22.
[34] M. Mazière, Overspeed Burst of Turboengine Disks, PhD dissertation, Mines ParisTech, 2007.
[35] C. Fressengeas, A.J. Beaudoin, M. Lebyodkin, L.P. Kubin, Y. Estrin, Dynamic strain aging: a coupled dislocation−solute dynamic model, Mater. Sci. Eng. A 400 (2005) 226–230.
[36] A. Marais, M. Mazière, S. Forest, A. Parrot, P. Le Delliou, Identification of a strain-aging model accounting for Lüders behavior in a C–Mn steel, Philos. Mag. 92 (28–30) (2012) 3589–3617.
[37] S. Gupta, A.J. Beaudoin, J. Chevy, Strain rate jump induced negative strain rate sensitivity (NSRS) in aluminum alloy 2024: experiments and constitutive modeling, Mater. Sci. Eng. A 683 (2017) 143–152.
[38] D. Caillard, Dynamic strain ageing in iron alloys: the shielding effect of carbon, Acta Mater. 112 (2016) 273–284.
[39] S.G. Hong, S.B. Lee, Mechanism of dynamic strain aging and characterization of its effect on the low-cycle fatigue behavior in type 316l stainless steel, J. Nucl. Mater. 340 (2) (2005) 307–314.
[40] J. Besson, G. Cailletaud, J.-L. Chaboche, S. Forest, Non-Linear Mechanics of Materials, Springer, 2009.
[41] U.F. Kocks, Laws for work-hardening and low-temperature creep, J. Eng. Mater. Technol. 98 (1) (1976) 76–85.
[42] H.D. Wang, Comportement mécanique et rupture des aciers au C–Mn en présence de vieillissement dynamique, PhD dissertation, Ecole Centrale Paris, Paris, 2011.
[43] J. Belotteau, C. Berdin, S. Forest, A. Parrot, C. Prioul, Mechanical behavior and crack tip plasticity of a strain aging sensitive steel, Mater. Sci. Eng. A 526 (2009) 156–165.
[44] F. Springer, C. Schwink, Quantitative investigations on dynamic strain aging in polycrystalline Cu–Mn alloys, Scr. Metall. Mater. 25 (1991) 2739–2744.
[45] H.D. Wang, C. Berdin, M. Mazière, S. Forest, C. Prioul, A. Parrot, P. Le-Delliou, Portevin–Le Chatelier (PLC) instabilities and slant fracture in C–Mn steel round tensile specimens, Scr. Mater. 64 (5) (2011) 430–433.
[46] J.R.G. da Silva, R.B. McLellan, Diffusion of carbon and nitrogen in BCC iron, Mater. Sci. Eng. 26 (1976) 83–87.
[47] L.P. Kubin, K. Chihab, Y. Estrin, The rate dependence of the Portevin–Le Chatelier effect, Acta Metall. Mater. 36 (10) (1988) 2707–2718.
[48] S.H. Fu, T. Cheng, Q.C. Zhang, Q. Hu, P.T. Cao, Two mechanisms for the normal and inverse behaviors of the critical strain for the Portevin–Le Chatelier effect, Acta Mater. 60 (19) (2012) 6650–6656.
[49] M. Mazière, H. Dierke, Investigations on the Portevin–Le Chatelier critical strain in an aluminum alloy, Comput. Mater. Sci. 52 (1) (2012) 68–72.
[50] P. Verma, G.S. Rao, P. Chellapandi, G.S. Mahobia, K. Chattopadhyay, N.C. Srinivas, V. Singh, Dynamic strain ageing, deformation, and fracture behavior of modified 9Cr–1Mo steel, Mater. Sci. Eng. A 621 (2015) 39–51.
[51] M. Mazière, S. Forest, Strain gradient plasticity modeling and finite element simulation of Lüders band formation and propagation, Contin. Mech. Thermodyn. 27 (2015).
[52] M. Mazière, C. Luis, A. Marais, S. Forest, M. Gaspérini, Experimental and numerical analysis of the Lüders phenomenon in simple shear, Int. J. Solids Struct. 106–107 (2017) 305–314.
[53] B. Max, B. Viguier, E. Andrieu, J.-M. Cloue, A re-examination of the Portevin–Le Chatelier effect in alloy 718 in connection with oxidation-assisted intergranular cracking, Metall. Mater. Trans. A 45A (2014) 5431–5441.
[54] Y. Bréchet, Y. Estrin, On a pseudo-Portevin–Le Chatelier effect, Scr. Metall. Mater. 31 (1994) 185–190.